Aerodynamic parametric analysis of an unconventional joined-wing aircraft configuration

Javier Pérez-Álvarez[1], Cristina Cuerno-Rejado[2] and José Meseguer[1]

Abstract

In this paper, the experimental results of an unconventional joined-wing aircraft configuration are presented. The test model uses two different wings, forward and rear, both joined in tandem and forming diamond shapes both in plant and front views. The wings are joined in such a way that it is possible to change the rear wing dihedral angle values and the rear wing sweep angle values in 25 different positions that modify the relative distance and the relative height between the wings. To measure the system aerodynamic coefficients it is necessary to perform wind tunnel tests. The data presented corresponds to the lift, drag and induced drag aerodynamic coefficients, as well as the aerodynamic efficiency and the parameter for minimum required power, from the calculated values of the lift and drag time series measured by a 6-axis force and torque sensor. The results show the influence on the aerodynamic coefficients of the rear wing sweep and dihedral angles parameters. As a main result, it can be concluded that, in general terms, the lift and induced drag aerodynamic coefficients values decrease as both the distance and height between the wings increase, on the other hand, the total drag aerodynamic coefficient decreases if the distance between the wings increases, but nevertheless shows a slight tendency to increase if the height of the rear wing increases, whereas the aerodynamic efficiency and the parameter for minimum required power increase if the distance between the wings increases.

Introduction

In the last 50 years, one of the major fields of innovation in aeronautical design is the pursuit of improvements for optimizing the aerodynamic and structural efficiency and the weight of aircraft.[1] Although the objective of improving the aerodynamic characteristics, and as a result the performance of the aircraft, has motivated designers to use the idea of configurations based on high aspect ratio wings, the problems of the weight of the structure, incremented by the increase of the required structural stiffness to accomplish the requirements entailed, have restricted the geometry to a safe design.

On the other hand, the rise in and instability of the cost of petroleum and its products (to its stabilization in 2012) and the continued growth of the commercial aviation market, are generating ever-increasing fuel costs. The corresponding impact on the direct operating costs (DOCs), producing a rise between 30% and 40%, has led to a search for innovating solutions in the design of both aircraft and propulsion that allow a reduction in costs by using more energetically efficient systems.[2]

To date, every single enhancement destined to improve the efficiency of aircraft has been carried out by preserving the conventional configuration, i.e. slender fuselage aircraft, mid and low wings, vertical and horizontal stabilizers attached to the tail cone, and wing-mounted or empennage-mounted engines. However, it appears that technological development levels where the investment in advances makes up for the results are reaching their own significant productive capacity limits. A clear example of

[1]IDR/UPM, ETSI Aeronáutica y del Espacio, Universidad Politécnica de Madrid, Madrid, Spain
[2]DAVE, ETSI Aeronáutica y del Espacio, Universidad Politécnica de Madrid, Madrid, Spain

this fact can be found in the recent developments of The Boeing Company, where its latest model, the Boeing 787 Dreamliner, is designed with the aim that 50% of the primary structure, including both the fuselage and wings, is made of composite, which results in, according to the company, using a 20% less fuel than any other aircraft of the same size in similar missions.

Likewise, there is a much clearer alternative that involves supporting the development of non-conventional geometric configurations,[3] which are already considered as real options by large aeronautical companies. The nonconventional configuration aircraft concept of Airbus shows what air transport could be like in the year 2050 or even in 2030 if the progress in existing technologies maintains its momentum. Such nonconventional configurations include extremely high aspect ratio wings, semi-embodied engines and a U tail aircraft.[4] The result is lower fuel consumption and a significant reduction in pollutant gases.

Within the abovementioned idea resides a nonconventional configuration model called the joined-wing configuration aircraft. This consist of a design that uses a forward wing and a rear wing that are joined in tandem so that it is diamond shaped both in top and front views. Figure 1 shows a simplified representation of this kind of configuration.

In 1979, Julian Wolkovitch,[5] in collaboration with J. L. Johnson, deputy director of the ACA Industries Dynamic and Stability Department, conducted some tests in a wind tunnel on a joined-wing aircraft configuration for agricultural purposes. The configuration, designed by the prototypes manufacturer Elbert L. Rutan (founder of Scaled Composites, Inc.), consisted of a propeller-driven aircraft with the rear wing joined to the mid span of the forward wing.

In 1989, the designs suggested by ACA industries, with the aid of the NASA Ames Research Center, were studied in a wind tunnel to measure the aerodynamic characteristics of the joined-wing model. The tests were conducted by modifying the NASA-AD1 aircraft,[6] preserving the fuselage and the engines in two different versions.

In early 2000, Boeing developed the SensorCraft joined-wing model[7,8] with the purpose of meeting the needs of the U.S.A.F. for the design of an aircraft with larger and better surveillance capacities. The key factors that determined the design of the SensorCraft aircraft were the need to keep 360° radar coverage over the aimed zone and to widen the capacities of the unmanned aircraft.

At the end of the first decade of the 21st century Air Force Research Laboratories (AFRL)

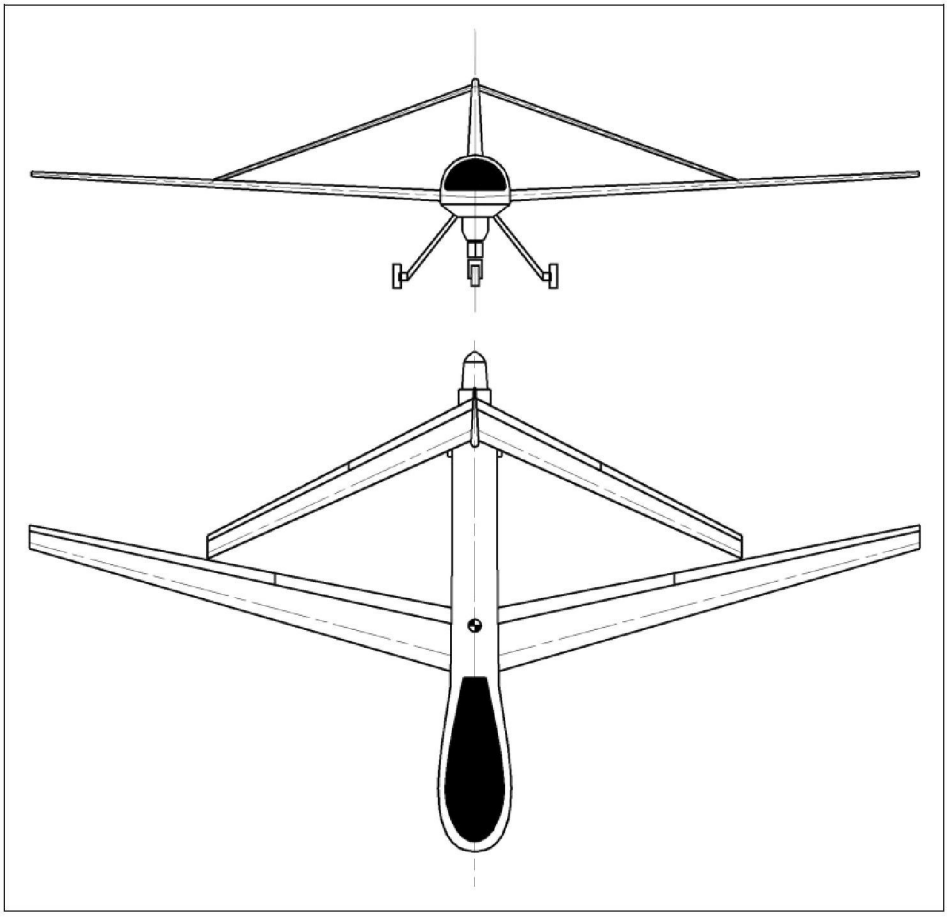

Figure 1. Simplified representation of the joined-wing configuration.

commended the research on the aerodynamic characteristics of the joined-wing model called Houck[9] to the Department of Aeronautics of the United State Air Force Academy. The model of study was based on the LRLE concept (long range, long endurance) within the unmanned aerial systems (UAS) environment.

From an aerodynamic standpoint, all research performed on this specific configuration, in the arrangement of the lifting surfaces, presents a direct influence on the lift, C_L, and drag, C_D, coefficients of the system.[2,5,7,10 12] In general, a significant reduction in the induced drag coefficient, C_{Di}, is presented as one of the most important advantages of the model.

The problem to reduce the induced drag of multiplanes systems (including the joined-wing configuration) was discussed by Prandtl[13] who provided formulas for the theoretical calculus of the aerodynamic efficiency using the general laws established by Munk.[14] Recent numerical investigation has demonstrated that the Munk's minimum induced drag theorems are also applicable to joined-wings and generic bi-wings.[15]

The Prandfl–Munk theory predicts that multiplanes systems configurations have lower induced drag than conventional configurations of similar span, total lift, and dynamic pressure.

In this context, Prandtl stated that the main idea for the minimization of induced drag is to reduce, as much as possible, the gradients of the circulation.

From this idea, Wolkovitch[5,16] conducted several studies where the advantages by the use of multiplanes systems are shown.

One of the advantages, that he demonstrated, was that (in tandem-wing configuration) the induced drag is less if the vertical gap between the front wing and the rear wing increases.

Secondly, Wolkovitch[5] confirmed with tests conducted in a wind tunnel that the Oswald efficiency factor, e, was greater than the one predicted by the Prandtl–Munk biplane theory.[14]

The analytical method of Prandtl–Munk produced as a result that the ratio of the Oswald efficiency factor, e, of the joined-wing configuration with respect to the equivalent monoplane was of the order of 1.05,[17] while the tests performed by Wolkovitch showed that the value was 1.09, ergo, 4% bigger than the one predicted by the Prandtl–Munk theory. On the basis of his research, Wolkovitch maintained that the classical theory disregarded the deflection of the wake over the forward wing, which leads to a reduction in the induced drag coefficient, C_{Di}, of the order of 5%, consequently resulting in the increase in the value of the efficiency factor.

In a similar way, from the aerodynamic point of view, other studies about the joined-wing model have assessed the optimal shape of the joint between wings[9,10] in order to determine its influence on the drag components (induced, pressure and friction).

As a conclusion, it can be established that, in general, all the studies show in their results a significant reduction in the induced drag coefficient of the joined-wing model. However, not every single one of them suggests aerodynamic aspects as the principal direct cause. The structural advantages of the joined-wing model,[5,18] as the reduction of weight (80–90% of the weight of the conventional wing) and the reduction of deflection of the wings, due the influence of the join of the forward wing and rear wing, give a higher aspect ratio resulting in a reduction in the induced drag.

On the other hand, all the previous studies agree in confirming the appearance of a significant increment of the overall lift of the aircraft, presenting better values of the maximum lift coefficient for level cruise flight, hence, improvements in aerodynamic efficiency.[5,19]

This situation makes the joined-wing model a suitable candidate for research and development in view of a future application in air transport, provided that the social obstacles that introducing such significant changes in the geometry of civil aircraft imply are overcome. Furthermore, and in a more immediate way, this kind of configurations are perfect for the UAS field of application, where the specific characteristics of this configuration can provide a great advantage.[7,8]

In view of the foregoing, the analysis of different configurations for the optimization of the model is posed as the objective, by evaluating how and in what way different variations of geometric parameters affect the main aerodynamic characteristics of the system.

This work is divided into three sections. In the first section, a conventional test setup design is undertaken where the parameters of the test model and test equipment are described. The next section shows how the aerodynamic coefficients of the joined-wing model change as a function of the design parameters, and in the last section of the article a final analysis is presented on the basis of the results of the previous sections.

Test setup

To conduct the different tests it is necessary to construct a physical model that allows the geometry of the different configurations to be adopted in a simple way. The test physical model is comprised of a forward wing semi-span and rear wing semi-span mock-ups, this being the basic configuration with its geometric parameters shown in Figure 2, both in front and top views.

The test model geometry is completely determined with the geometric parameters shown in Table 1.

In choosing the basic values of the geometric parameters defined in Table 1, the following considerations about the technical and functional aspects

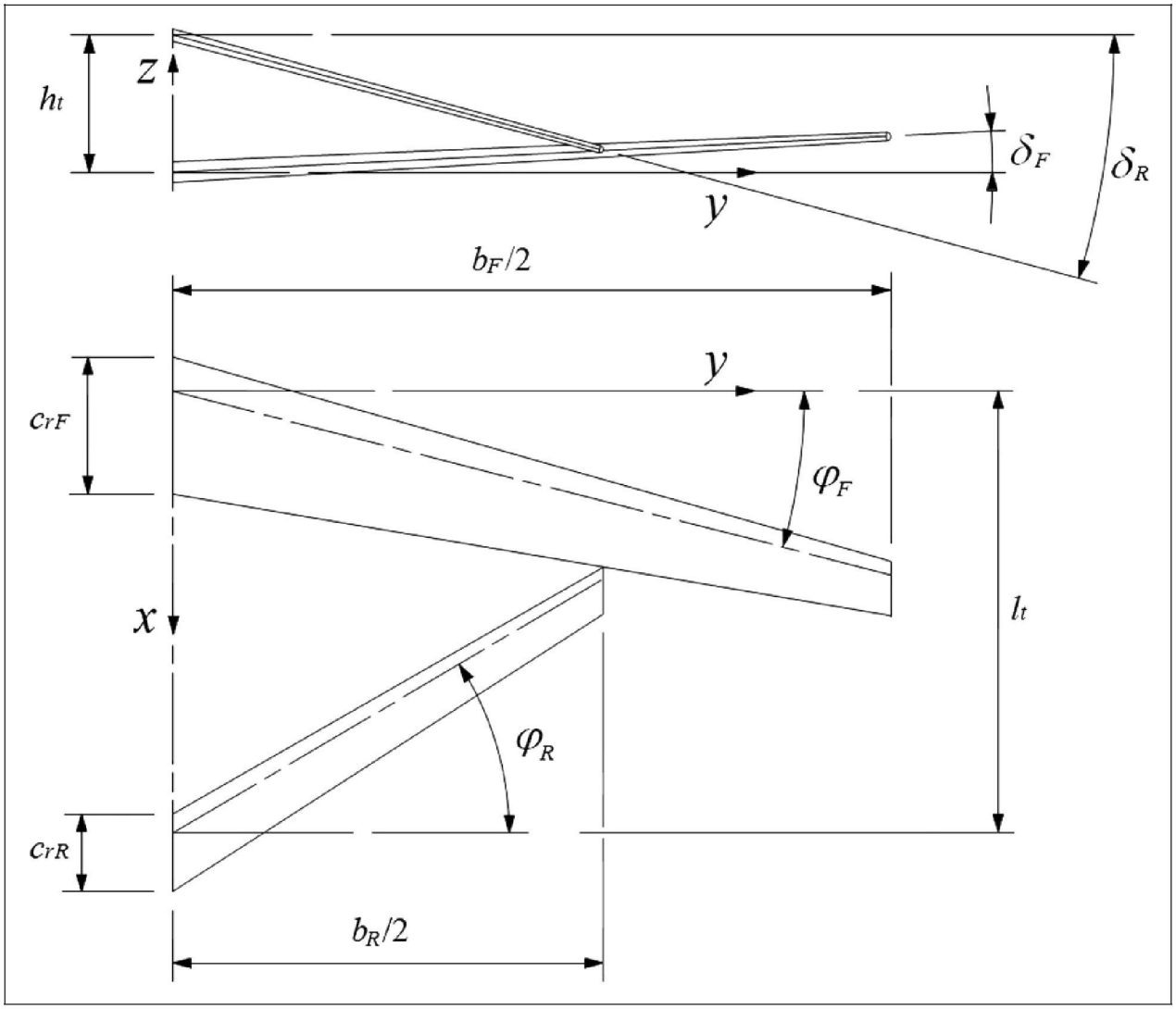

Figure 2. Top and front views of the simplified representation of the unconventional joined-wing aircraft configuration test model.

related to the nature of the test have been kept in mind:

- The forward wing span value and the forward wing root chord value have been determined to avoid corrections by geometric blockage in the wind tunnel test section. As it is well known, for this to happen, the relation between the test model front area and the wind tunnel test section cross sectional area must be less than 7.5%.[20] This relation is of the order of 4% for the test model.
- In selecting the rear-forward span ratio parameter value, B, the studies conducted by other authors have been considered, which, after analyzing different configurations, suggest that the optimal value of this parameter is between 0.6 and 0.7.[4,9]
- The assigned value to the forward wing sweep angle, in general, differs from the one defined by Smith and Stonum.[6] Even though the majority of authors study configurations near to 30°, in the present work, the study of lower values was chosen; firstly to find more suitable situations for the purpose of this study and secondly due to the geometric constraints and speed in the test chamber.
- The type of joint employed to attach both wings together is a rigid joint, which was selected when considering the best tradeoff between strength and stiffness[21] (Figure 3).
- Finally, when choosing the airfoil, constructive, endurance, and aerodynamic aspects were considered. The choice of a symmetric airfoil simplifies the manufacturing of the wings. Relatively higher thickness provides greater stiffness to the assembly and, from the aerodynamic point of view, as known, relative thicknesses between 12% and 15% provide a higher value of the maximum lift coefficient.

Furthermore, the NACA 0015 airfoil shows an acceptable performance for low Reynolds numbers.[22]

As a result the values of the basic geometric parameters for the forward and rear wings have been established and are presented in Table 2.

Table 1. Geometric parameters for the test model definition.

Parameter	Definition
b_F	Forward wing span
λ_F	Forward wing taper ratio
c_{rF}	Forward wing root chord
φ_F	Forward wing sweep angle
δ_F	Forward wing dihedral angle
λ_R	Rear wing taper ratio
c_{rR}	Rear wing root chord
φ_R	Rear wing sweep angle
δ_R	Rear wing dihedral angle
B	Rear-forward span ratio
l_t	Distance between wings
h_t	Height between wings

Table 2. Test model values of geometric parameters.

Parameter	Value
b_F	1.56 m
λ_F	0.40
c_{rF}	0.158 m
φ_F	15°
δ_F	3°
B	0.60
b_R	0.93 m
λ_R	0.60
c_{rR}	0.09 m
φ_R	See Table 3
δ_R	See Table 3

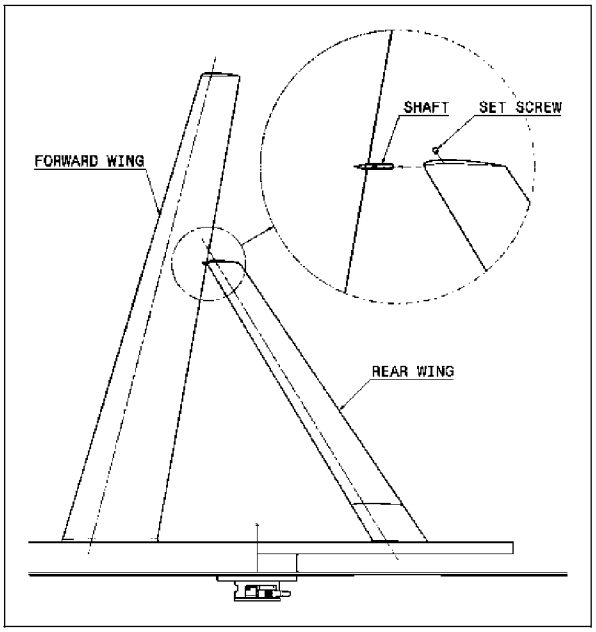

Figure 3. Scheme showing the rigid joint between the rear wing and the forward wing. The detail shows binding by a shaft, fixed to the front wing, and attached on the rear wing by a screw.

Table 3. Study configurations as a function of the rear wing sweep angle, φ_R (°), and the rear wing dihedral angle, δ_R (°).

	Rear wing sweep angle, φ_R (°)				
	−10	−15	−20	−25	−30
Rear wing dihedral angle, δ_R (°)					
−25	JWC_{11}	JWC_{12}	JWC_{13}	JWC_{14}	JWC_{15}
−20	JWC_{21}	JWC_{22}	JWC_{23}	JWC_{24}	JWC_{25}
−15	JWC_{31}	JWC_{32}	JWC_{33}	JWC_{34}	JWC_{35}
−10	JWC_{41}	JWC_{42}	JWC_{43}	JWC_{44}	JWC_{45}
−5	JWC_{51}	JWC_{52}	JWC_{53}	JWC_{54}	JWC_{55}

All the study configurations are obtained by keeping the forward wing basic geometry constant and modifying two parameters of the rear wing geometry: the dihedral angle, δ_R, and the sweep angle, φ_R. As a result, 25 different test configurations appear (Table 3).

For every testing configuration, each rear wing is an assembly of two pieces: a basic piece (mark 3, Figure 4) and a partial rear wing (mark 2, Figure 4).

The junction of the forward wing (mark 1, Figure 4) with the rear wing is a fixed point, so the length of each rear wing is different in function of its position on the turntable (mark 4, Figure 4). However, the rear wing span, b_R, and rear-forward span ratio parameter, B, are constant.

The variation of these parameters implies changes to the rear wing position in relation to the forward wing (Figure 5). The variation of the dihedral angle modifies the position in height of the rear wing, h_t, decreasing this height if the dihedral angle decreases in absolute value. However, an increase in the variation of the sweep angle modifies the relative position of both wings, l_t, decreasing the distance between them.

The height values, h_t, and relative distance between wings values, l_t, are expressed as follows

$$h_t = B\, l_F \cos\delta_F \cos\phi_F (\tan\delta_F - \tan\delta_R) \tag{1}$$

$$l_t = B\, l_F \cos\delta_F \cos\phi_F (\tan\phi_F - \tan\phi_R) + \frac{1}{4} c_{tR} + \frac{3}{4} c_{rF}[B(\lambda_F - 1) + 1] \tag{2}$$

where l_F corresponds to the forward wing non-projected semi-length, λ is the forward wing taper ratio, c_{tR} is the rear wing tip chord, c_{rF} is the forward wing root chord, δ_F, φ_F, δ_R, and φ_R are the dihedral

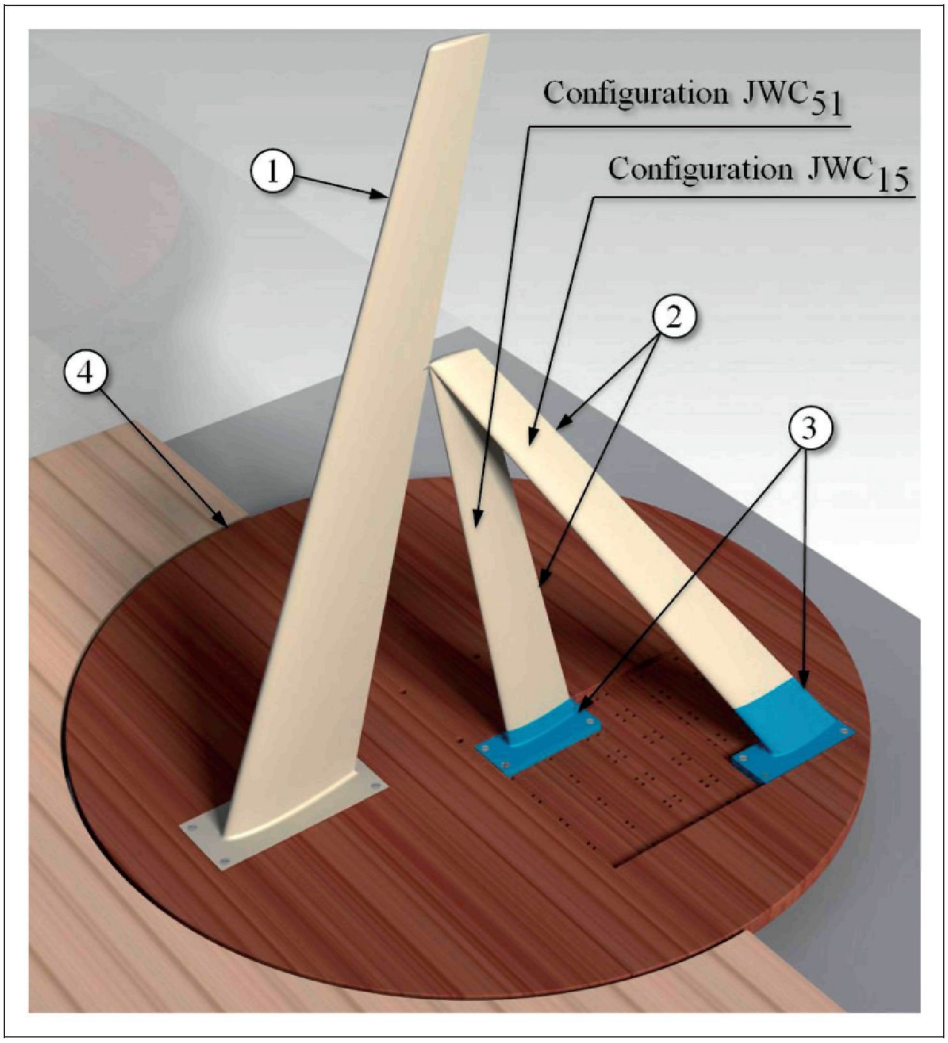

Figure 4. Sketch of the experimental set-up showing the junction of the forward wing (1) with the rear wing (2, 3) and fixed to the turntable (4). The figure shows two different configurations.

angle and the sweep angle on the 1/4 chord line of the forward and rear wing respectively, and B is the rear-forward span ratio, expressed as

$$B = \frac{b_R}{b_F} \tag{3}$$

The rear wing position values (height and distance) are nondimensional values related to the JWC_{15} configuration position which corresponds to a dihedral angle value of $\delta_R = -25°$ and a sweep angle value of $\varphi_R = -30°$, according to

$$\overline{h_t} = \frac{h_t}{h_{t\mathrm{JWC}_{15}}} \tag{4}$$

$$\overline{l_t} = \frac{l_t}{l_{t\mathrm{JWC}_{15}}} \tag{5}$$

Using expressions (1) and (2), the dimensionless height values, $\overline{h_t}$, and dimensionless distance values, $\overline{l_t}$, are shown in Tables 4 and 5.

To measure the system aerodynamic coefficients, the development of tests in a wind tunnel is necessary.

The A9 Tunnel of the "*Instituto* IDR/UPM" is an open return wind tunnel with a closed test section and open-circuit flow (Eiffel type). As can be seen in Figure 6, the A9 Tunnel is comprised of an inlet contraction (1), test section (2), and diffuser (3), which also acts as an adapter for the drive section where the fans are (4). The test section is about 3 m long with a cross section of 1.5 m width and 1.8 m height.

Before measuring the joined-wing model in the A9 Tunnel, the study of the behavior of the flow inside the test section in order to determine the turbulence intensity distribution, I_{Ux}, has been considered.

To determine the turbulence intensity, the velocity of the wind inside the test section, empty with no model, has been measured using a hot-wire anemometry equipment and an adjustable traverse guides system.

To obtain a wide spatial resolution, the velocity has been measured in 132 points contained on the cross section of the test section, distributed in a matrix of

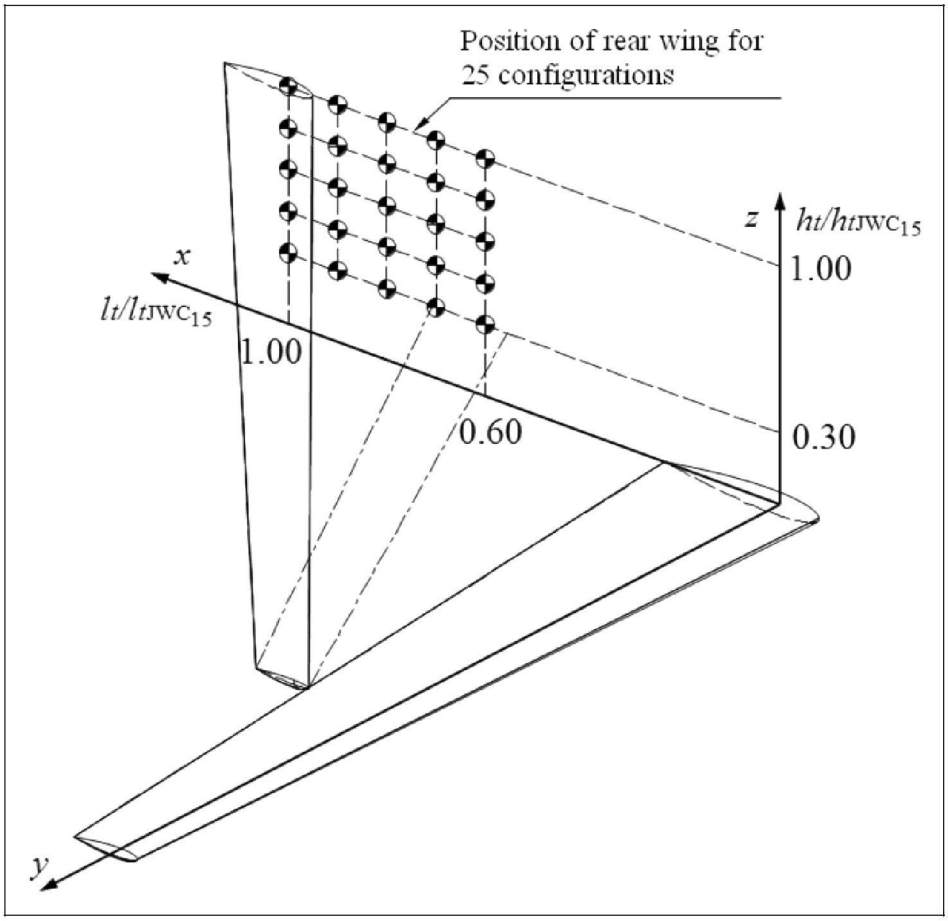

Figure 5. Drawing of the rear wing position in relation to the forward wing.

Table 4. Values of the dimensionless height, $\overline{h_t}$, as a function of the rear wing dihedral angle, δ_R (°).

	Rear wing dihedral angle, δ_R (°)				
	−5	−10	−15	−20	−25
$\overline{h_t}$	0.30	0.40	0.60	0.80	1.00

Table 5. Values of the dimensionless distance, $\overline{l_t}$, as a function of the rear wing sweep angle, φ_R (°).

	Rear wing sweep angle, φ_R (°)				
	−10	−15	−20	−25	−30
$\overline{l_t}$	0.60	0.70	0.80	0.90	1.00

11 rows and 12 columns (Figure 7), with a measuring time of $T_U = 120$ s at each point, a frequency of $f_U = 1000$ Hz and a wind tunnel speed measured with hot-wire anemometry equipment in the test section of $U_U = 25$ m/s.

Once the speed time series at each point has been obtained, it is possible to establish the turbulence intensity value, which does not exceed the value of 3% in the center of the test section, but is greater (>3%) near the walls (about 50 mm).

Although these values are greater than the required ones for aircraft aerodynamic tests (<0.5%),[19] they are acceptable for their application in the field of UAS.

The normal operating altitude of UAS, in the most general case and for Class I and mini and small categories,[23] is lower than 1500 m where the settings of the atmosphere are due to atmospheric boundary layer (ABL). The ABL is caused by the interaction of the geostrophic wind with the obstacles of the Earth's surface. The interaction occurs in two primary forms: mechanical and thermal. The mechanical interaction is produced from the friction exerted by the wind against the ground surface which results in a profile of average speed (10–20 m/s) that varies with height. In the lowest atmosphere the level of turbulence intensity (based on the average wind speed) is intimately related to the velocity.

In the case of UAS, the reference speed is the speed of flight (20–50 m/s), so that the turbulence intensity is between 5% and 15%, being these levels greater than those of conventional commercial aviation.

To conduct the test, the model is installed over a Newport RV80PP angular position sensor model (high accuracy of 0.01°) that allows the automatic

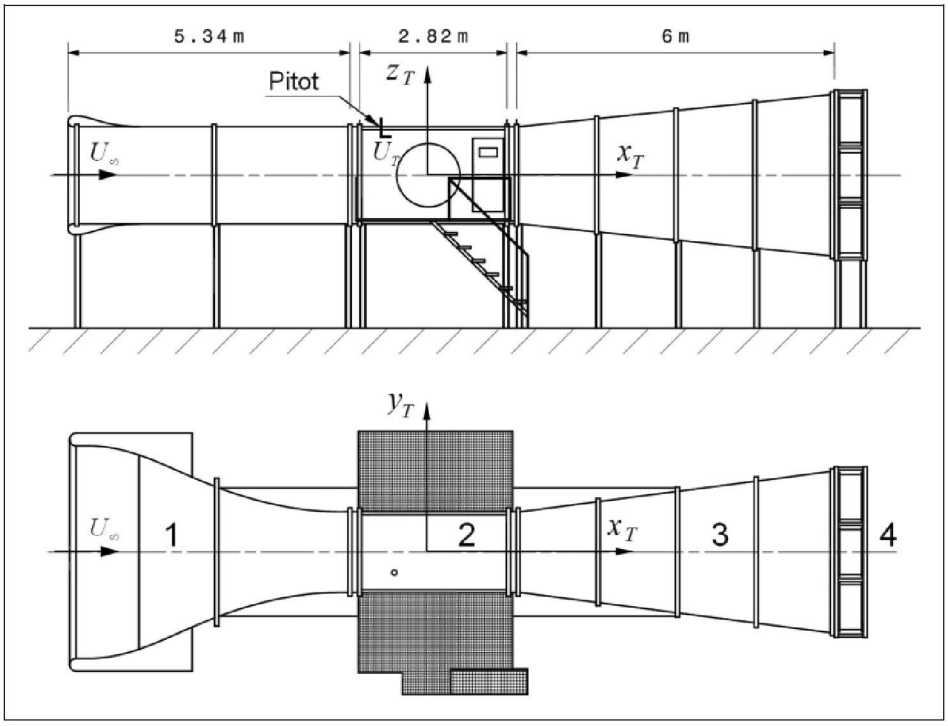

Figure 6. Front and top drawing views of the A9 Tunnel: (1) contraction, (2) test section, (3) diffuser/adapter, and (4) drive section/fans.

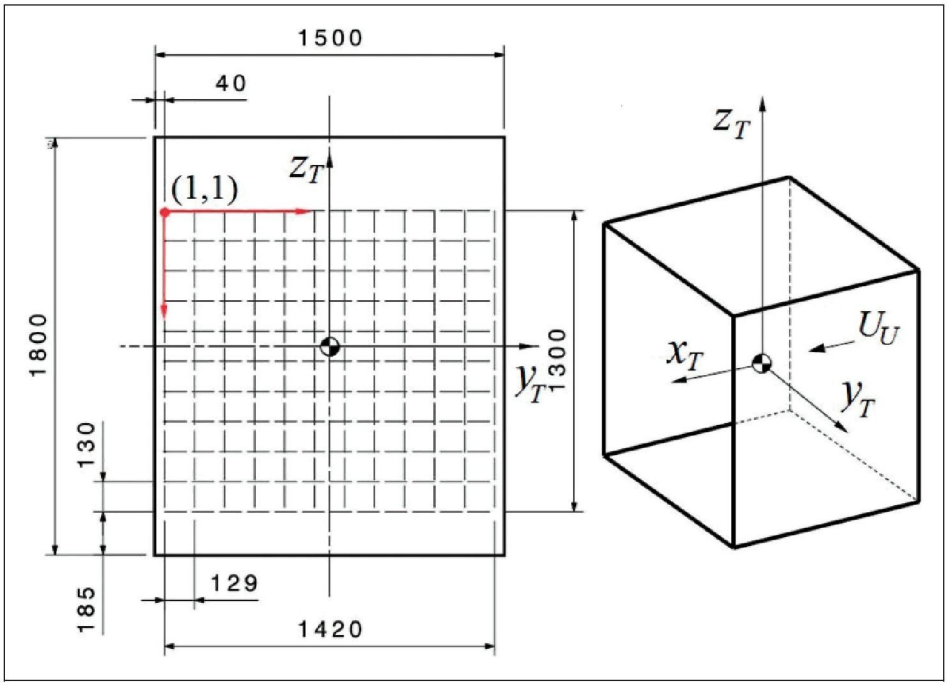

Figure 7. Velocity points matrix for the determination of the turbulence intensity.

spin for the loads measure at different angles of attack to be studied (Figure 8). The total loads measure on the test model is performed by a Delta force sensor SI-330-30 of Ati Industrial Automotion with detecting ranges, in axes x_T and y_T directions (Figure 7), of 330 N and a resolution of 1/16 N, which makes it possible to calculate the aerodynamic lift, L, aerodynamic drag, D, and the pitching moment, M_y, acting on the model.

The tunnel parameters to obtain the aerodynamic forces over the test model are:

- Velocity of the free-stream in the tunnel: $U = 25$ m/s

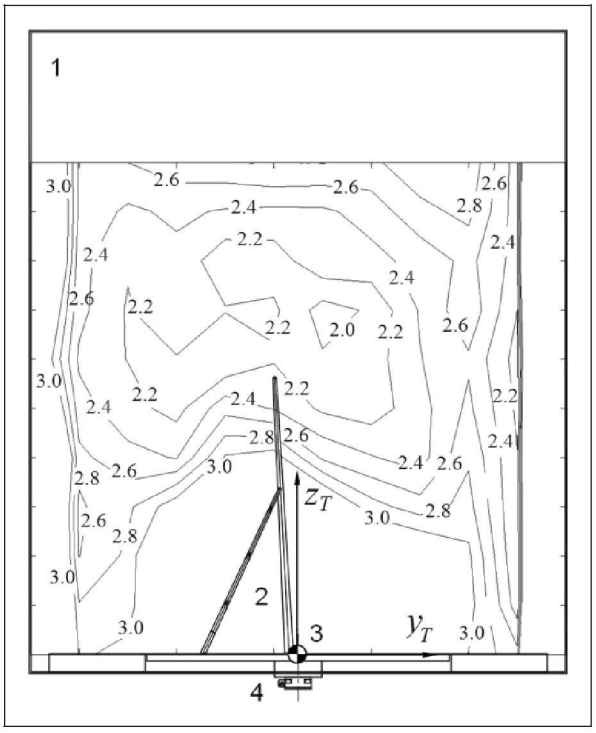

Figure 8. Test model assembly diagram in the A9 Tunnel test section where the turbulence intensity contour lines distribution is shown: (1) test section, (2) test model, (3) spin sensor, and (4) load sensor.

- Range of angles of attack: $\alpha = [-15°, 15°]$, at intervals of 1°
- Measuring frequency: $f = 1000$ Hz
- Measuring time: $T = 120$ s
- Reynolds number based on front wing mean aerodynamic chord: $Re = 250000$

Test results

Through aerodynamic analysis, it is possible to get optimum configuration of the joined-wing model from the point of view of the position of the rear wing, in order to analyze the best performance and flight characteristics of a joined wing aircraft in the preliminary design stage.

Specifically, the experimental analysis is aimed at defining the basic aerodynamic coefficients of lift, C_L, and drag, C_D, evaluated from the time series values of lift, L, and drag, D, measured by force and torque sensors according to the expressions

$$C_L = \frac{L}{q\,b\,\bar{c}} \tag{6}$$

$$C_D = \frac{D}{q\,b\,\bar{c}} \tag{7}$$

where q denotes the dynamic pressure, b is the effective span,[5] and $\bar{c}$ is the effective wing mean aerodynamic chord of the front and rear wing ensemble, values according to

$$b = \frac{1}{2}\left[\left(\frac{b_F}{\cos\delta_F \cos\varphi_F}\right) + \left(\frac{b_R}{\cos\delta_R \cos\varphi_R}\right)\right] \tag{8}$$

$$\Lambda = \frac{\Lambda_F\left(\frac{S_F}{S_R}\right) + \Lambda_R\left(\frac{S_R}{S_F}\right)}{\left(\frac{S_F}{S_R}+1\right) + \left(\frac{S_R}{S_F}+1\right)} \tag{9}$$

$$\bar{c} = \frac{b}{\Lambda} \tag{10}$$

where S_F is the forward wing area, S_R is the rear wing area, and Λ is the effective aspect ratio.[5,24]

The effective span, b, is defined as the mean of the not projected lengths of the quarter-chord lines of the forward wing and the rear wing. The effective aspect ratio, Λ, is a geometric relation and takes into consideration the individual wings surface area, but it does not account for any aerodynamic coupling between the joined wings.

In addition, the associated aerodynamic coefficients, induced drag coefficient, C_{Di}, and the aerodynamic efficiency, E, are also determined, and calculated by the expressions

$$C_{Di} = \frac{C_L^2}{\pi\,\Lambda\,e} \tag{11}$$

$$E = \frac{C_L}{C_D} \tag{12}$$

where e is the induced drag efficiency factor corrected for the Wlkovitch's joined-wing model by the effect of the forward and rear sweep angle[5] and given by

$$e = e_t[1 + 0.0435\,(\tan\varphi_F + \tan\varphi_R)] \tag{13}$$

where e_t is the theoretical induced drag efficiency factor. This factor was estimated by Letcher[25] for nonplanar wings; v-wings and diamond-wings. Several years after, DeYoung[26] developed a generalized equation for arbitrary cross-sectional wing forms, including diamond box-wing and partial span diamond box-wing,[25] expressed as

$$e_t|_{B=0.6} = 0.04H^3 + 0.18H^2 + 0.1H + 1 \tag{14}$$

where H[26] is the dimensionless maximum height according to

$$H = \frac{h_t}{b_F} \tag{15}$$

As can be seen in equation (13), the value of e is a function of the forward and rear wing sweep angle and as can be seen with equation (14), it has a strong dependence on the height between the

forward wing and the rear wing.[26] This value is shown in Table 6.

The values of the lift, C_L, and drag, C_D, coefficients are represented in Figure 9, and the values of aerodynamic efficiency, E, and the factor $C_L^{3/2}/C_D$ for minimum required power are depicted in Figure 10, where the variation with respect to the angle of attack, α, can be seen.

Similarly, the variation of the lift, C_L, and, $C_L^{3/2}$, coefficients as a function of the drag coefficient, C_D, are represented in Figure 11, and the dashed line is the tangent to the curve being the contact point the maximum value of $C_L^{3/2}/C_D$, i.e. minimum required power point. These figures correspond to the JWC_{15} configuration, i.e. for rear wing dihedral angle $\delta_R = -25°$, and for rear wing sweep angle $\varphi_R = -30°$.

Table 6. Induced drag efficiency factor values, e, as a function of the rear wing sweep angle, φ_R (°) and the rear wing dihedral angle, δ_R (°).

	Rear wing sweep angle, φ_R (°)				
	−10	−15	−20	−25	−30
Rear wing dihedral angle, δ_R (°)					
−25	1.039	1.044	1.048	1.052	1.057
−20	1.035	1.039	1.043	1.048	1.053
−15	1.031	1.035	1.039	1.044	1.048
−10	1.027	1.031	1.035	1.040	1.045
−5	1.024	1.028	1.032	1.037	1.041

On the other hand, the graphs of the aerodynamic coefficients, $\overline{C_L}$, $\overline{C_D}$, and $\overline{C_{Di}}$ are represented as a function of the rear wing sweep angle, φ_R, and the rear wing dihedral angle, δ_R, for different values of the angle of attack, α where $\overline{C_L}$, $\overline{C_D}$, and $\overline{C_{Di}}$ are normalized with respect to the values of the JWC_{15} configuration ones ($C_{L_{15}}$, $C_{D_{15}}$, and $C_{Di_{15}}$).

In Figure 12 the variation of the normalized lift coefficient, $\overline{C_L}$, is shown, where it can be seen that the value is greater when the rear wing is closer to the front wing; this is due to the front wing causes downwash[5] on the rear wing, and the rear wing induces upwash[5] on the front wing. Stating that, the total lift of a joined-wing is lower than the simple sum of the front and rear wings lifts, because of the downwash effect on the rear wing that reduces the lift.

In Figure 13 the normalized total drag coefficient value, $\overline{C_D}$, is represented, and shows that its value presents little dependence of the dihedral angle of the rear wing, and it seems to depend mainly on the separation, l_t, between the wings.[24] On the other hand, the figure shows that the total drag coefficient value increases if the height between the wings decreases. This may be due to interference from the front wing flow impinging on the rear wing.

In Figure 14 the normalized induced drag coefficient value, $\overline{C_{Di}}$, is shown. The behavior of this value is inversely proportional to the value of the induced drag efficiency factor, e, which, as stated, increases as the height of the rear wing increases.

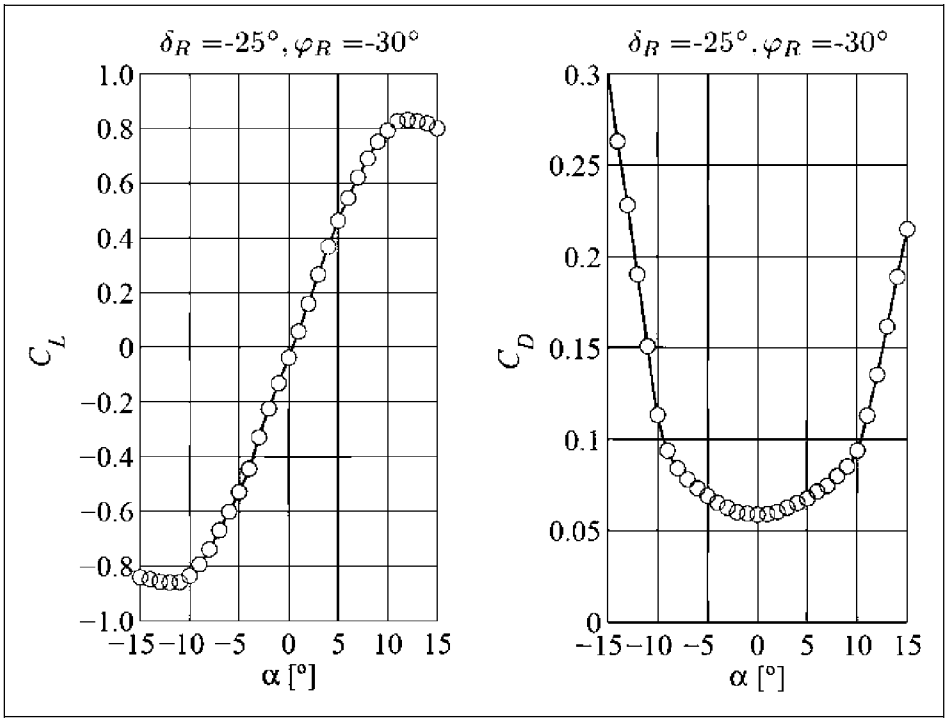

Figure 9. Variation of the lift, C_L, and drag, C_D, coefficients as a function of the angle of attack, α, for rear wing dihedral angle $\delta_R = -25°$ and rear wing sweep angle $\varphi_R = -30°$. Free-stream Reynolds number $Re = 250{,}000$.

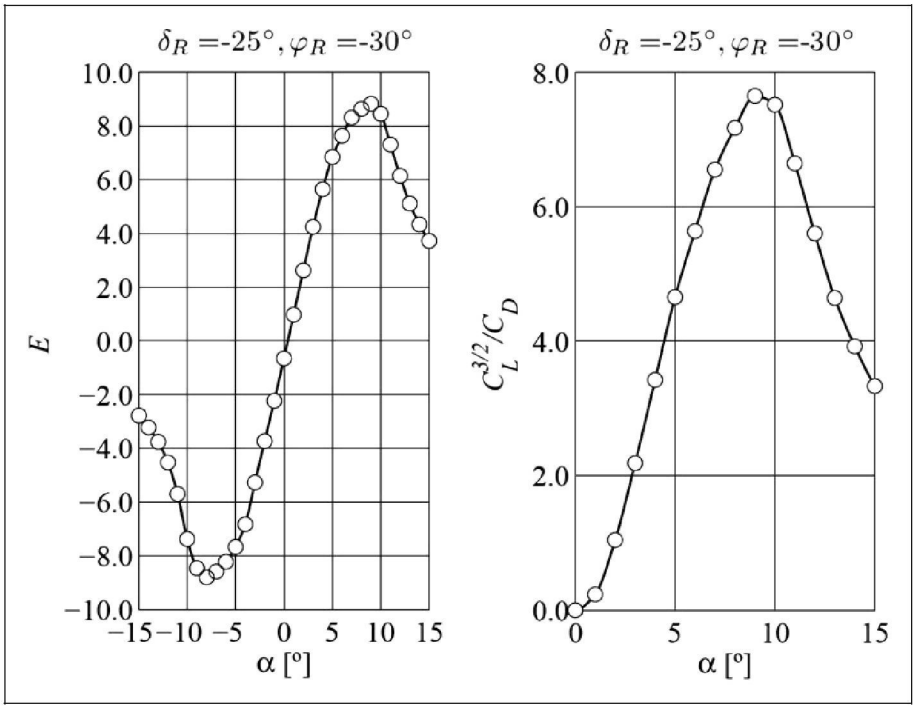

Figure 10. Variation of the aerodynamic efficiency, E, and factor $C_L^{3/2}/C_D$ for minimum required power, as a function of the angle of attack, α, for rear wing dihedral angle $\delta_R = -25°$and rear wing sweep angle $\varphi_R = -30°$. Free-stream Reynolds number $Re = 250{,}000$.

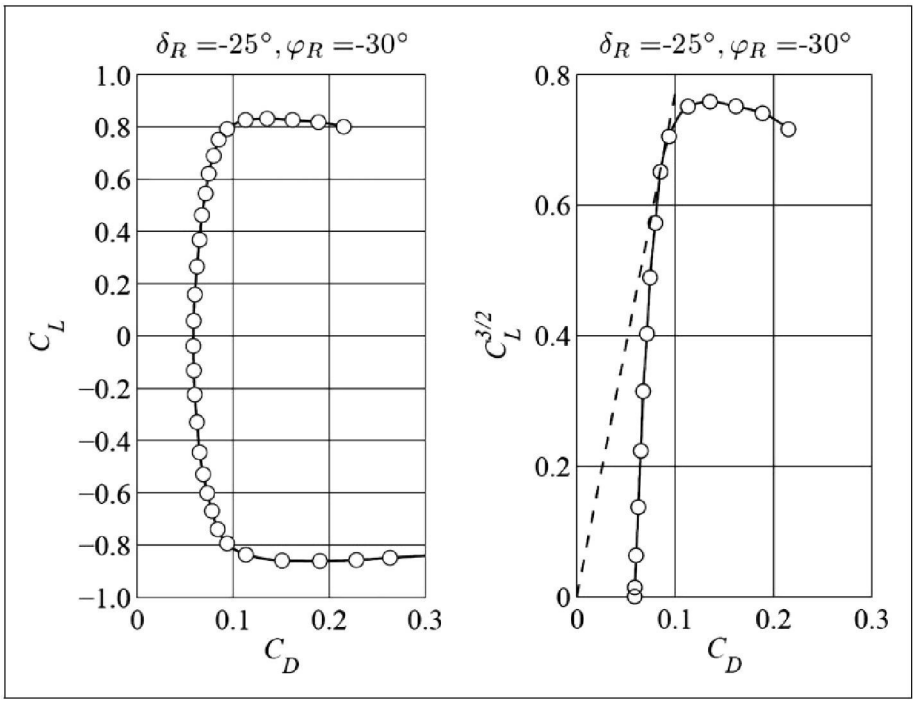

Figure 11. Variation of the lift coefficient, C_L, and coefficient, $C_L^{3/2}$, as function of the drag coefficient, C_D, for rear wing dihedral angle $\delta_R = -25°$ and rear wing sweep angle $\varphi_R = -30°$. The dashed line shows the maximum $C_L^{3/2}/C_D$ point. Free-stream Reynolds number $Re = 250{,}000$.

In each figure, and for each angle of attack, the maximum and minimum values for each coefficient are shown, as well as the values for each coefficient of the reference configuration.

In Figure 15, the maximum value of the aerodynamic lift and minimum value of the drag are represented as a function of the rear wing sweep angle and for each value of the rear wing dihedral angle.

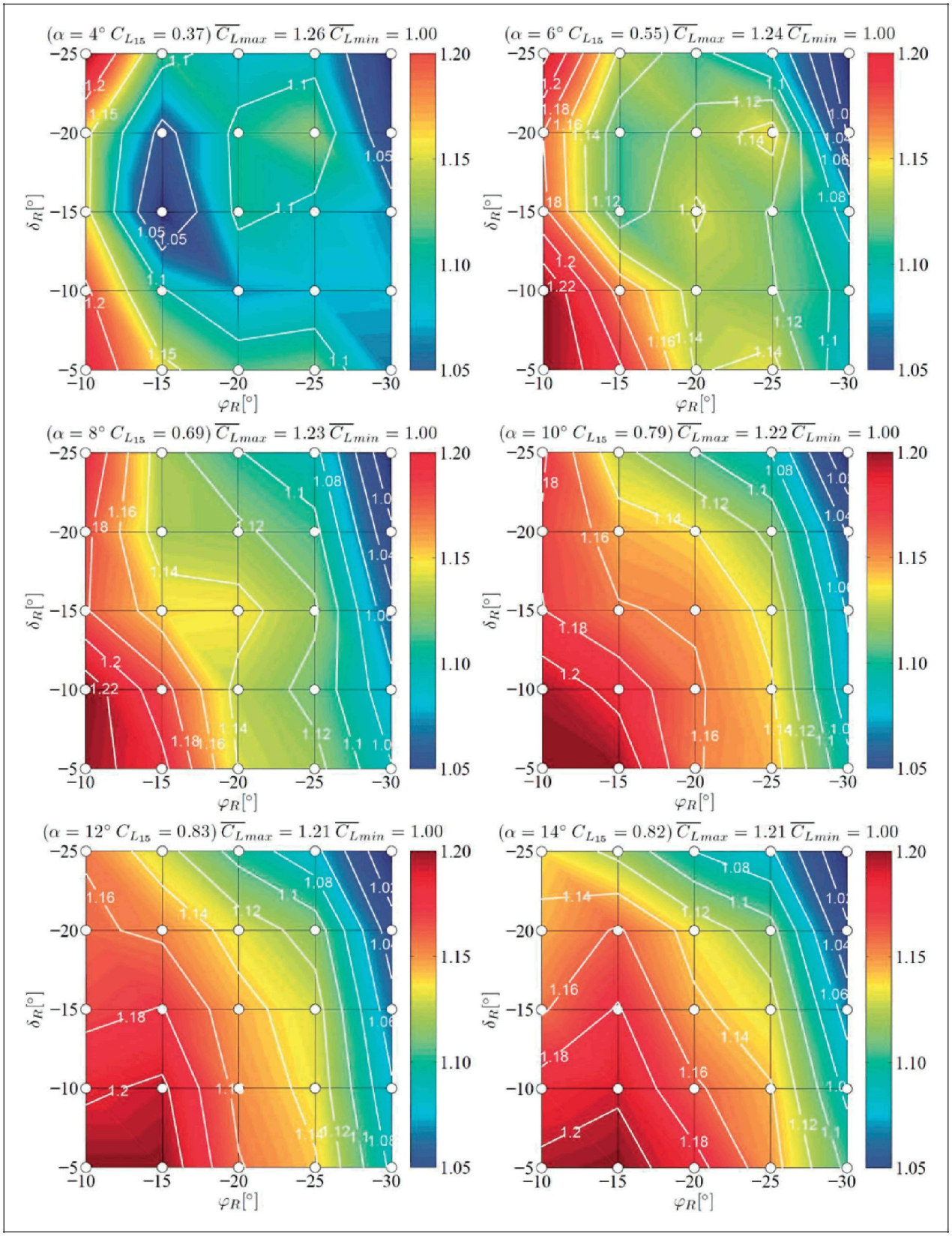

Figure 12. Variation of the lift coefficient, $\overline{C_L}$, as a function of the rear wing sweep angle, φ_R, and the rear wing dihedral angle, δ_R, for each angle of attack, α. Free-stream Reynolds number $Re = 250{,}000$.

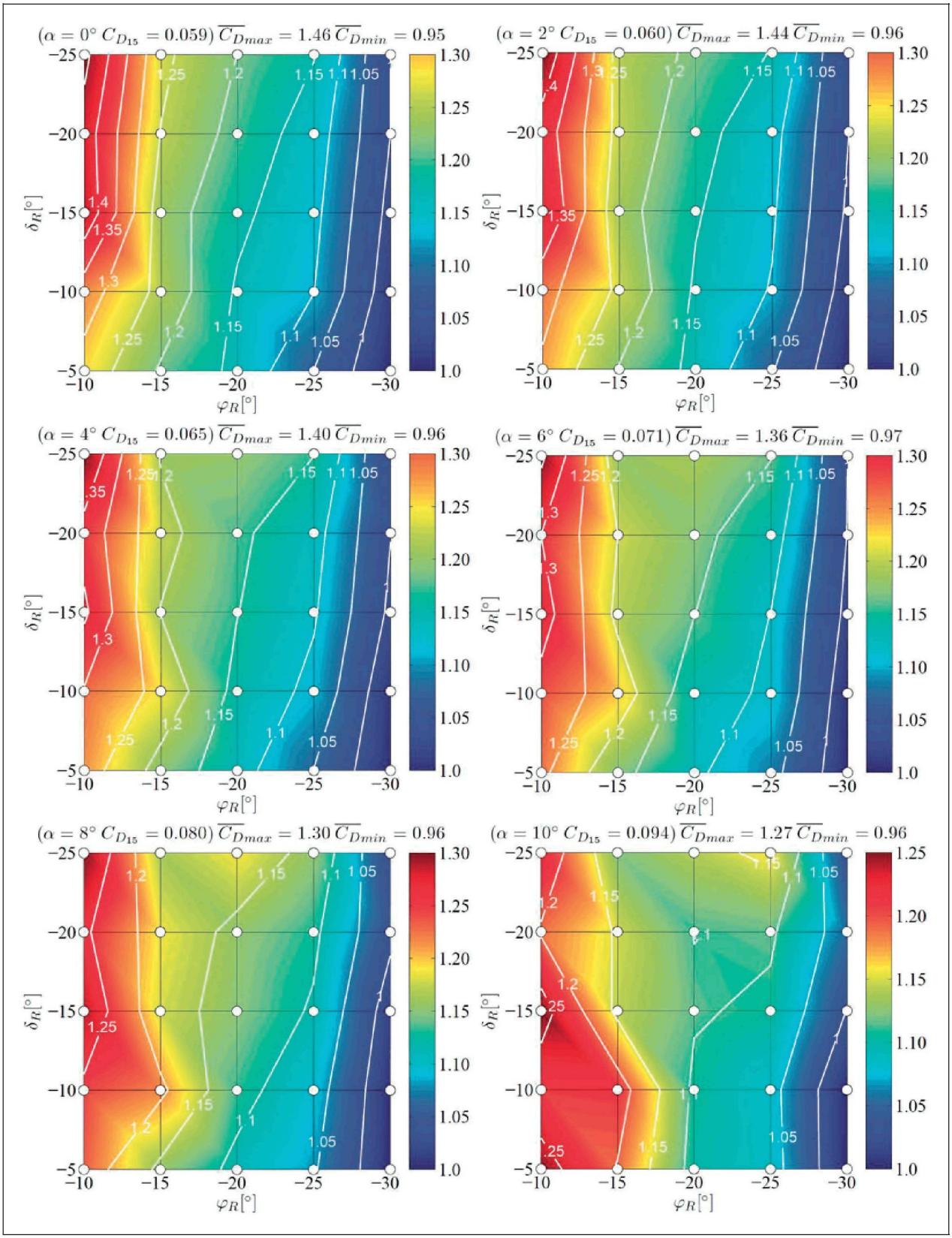

Figure 13. Variation of the drag coefficient, $\overline{C_D}$, as a function of the rear wing sweep angle, φ_R, and the rear wing dihedral angle, δ_R, for each angle of attack, α. Free-stream Reynolds number $Re = 250{,}000$.

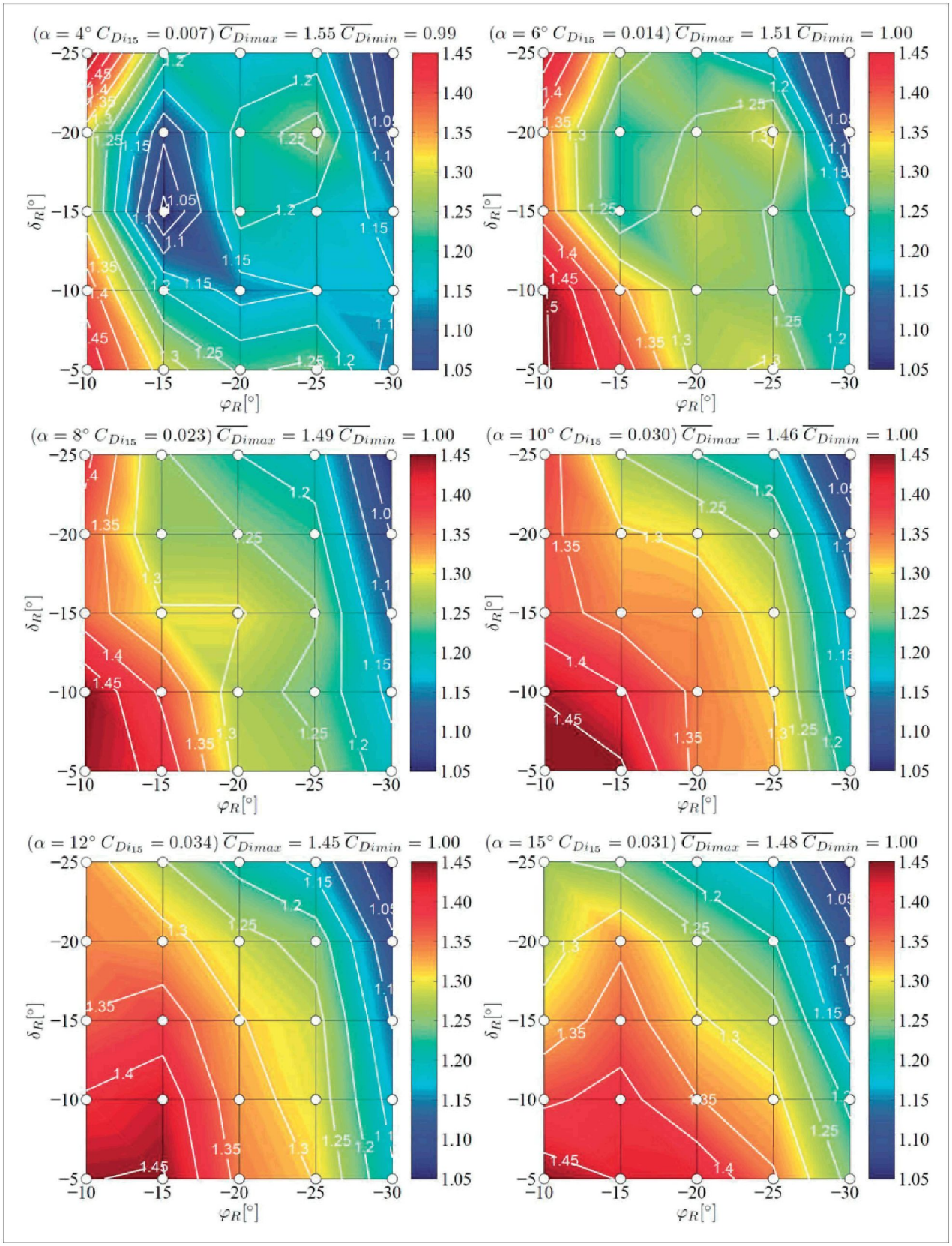

Figure 14. Variation of the induced drag coefficient, $\overline{C_{Di}}$, as a function of the rear wing sweep angle, φ_R, and the rear wing dihedral angle, δ_R, for each angle of attack, α. Free-stream Reynolds number $Re = 250{,}000$.

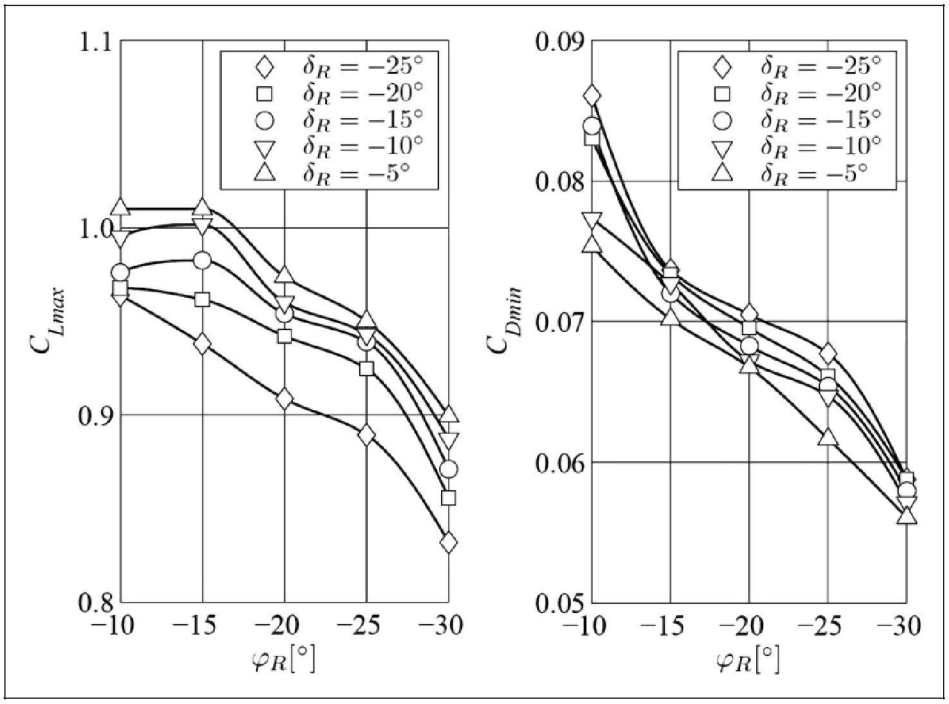

Figure 15. Variation of the maximum lift, $C_{L_{max}}$, and minimum drag, $C_{D_{min}}$, coefficients as a function of the rear wing sweep angle, φ_R, and the rear wing dihedral angle, δ_R. Free-stream Reynolds number $Re = 250{,}000$.

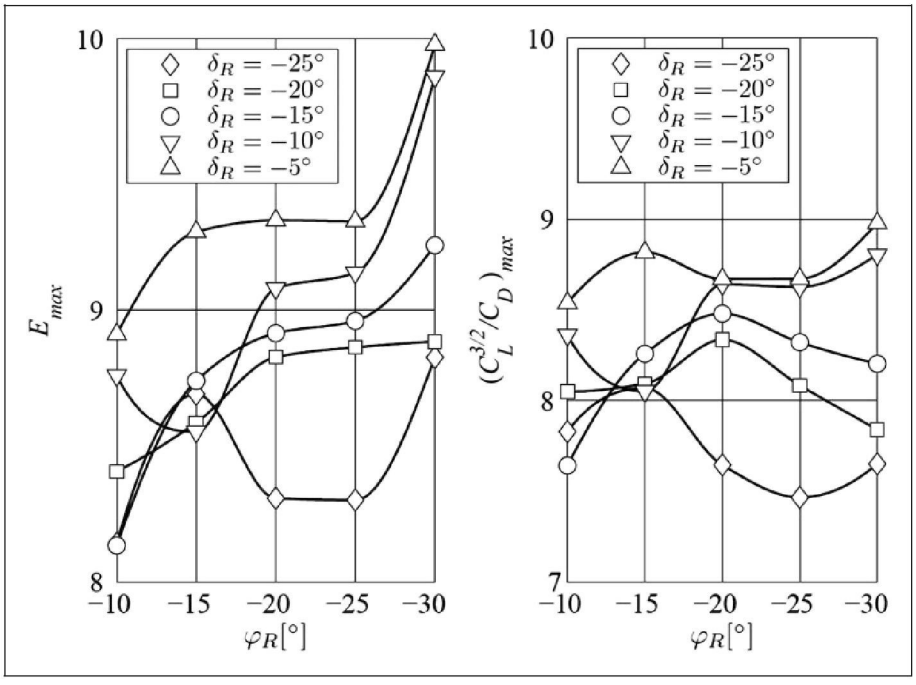

Figure 16. Variation of the maximum aerodynamic efficiency, E_{max}, and maximum $C_L^{3/2}/C_D$ for minimum required power coefficients as a function of the rear wing sweep angle, φ_R, and the rear wing dihedral angle, δ_R. Free-stream Reynolds number $Re = 250{,}000$.

Finally, in Figure 16 the maximum value of the aerodynamic efficiency and maximum value of the parameter $C_L^{3/2}/C_D$ for minimum required power coefficients are represented as a function of the rear wing sweep angle and for each value of the rear wing dihedral angle.

Conclusions

In view of the results, it has been proven that the variation in the aerodynamic coefficients is more pronounced as the rear wing sweep angle, φ_R, is modified rather than when the rear wing dihedral angle, δ_R, is

modified. While the rear wing sweep angle increments produce variations of up to 20% in the lift coefficient value, C_L, and up to 40% in the drag coefficient value, C_D, dihedral angle increments produce only variations from up to 2% in the lift coefficient value and up to 10% in the drag coefficient value. It seems clear that, although modifications in distance, l_t, and height, h_t, of the rear wing have an evident influence on the aerodynamic coefficients of the model, this influence is greater in the first case. On the other hand, depending on the aerodynamic coefficient, the variation in its value presents different behaviors.

The lift coefficient tends to be higher as the rear wing dihedral and sweep angles are reduced, as show in Figure 12. In general, the JWC_{51} configuration ($\delta_R = -5°$, $\varphi_R = -10°$) presents maximum values up to 20% higher than the JWC_{15} configuration ($\delta_R = -25°$, $\varphi_R = -30°$) presents. In conclusion, the lift coefficient decreases as the distance and the height of the rear wing increase.

The drag coefficient tends to be lower as the rear wing dihedral angle decreases and the sweep angle increases (both in absolute value), as shown in Figure 13. In general, the JWC_{55} configuration ($\delta_R = -5°$, $\varphi_R = -30°$) presents minimum values up to 40% lower than the JWC_{11} configuration ($\delta_R = -25°$, $\varphi_R = -10°$). In conclusion, the total drag coefficient decreases as the distance of the rear wing increases and the height of the rear wing decreases.

The induced drag coefficient tends to be lower as the rear wing dihedral and the sweep angles increase (both in absolute value) (Figure 14). In general, the JWC_{15} configuration ($\delta_R = -25°$, $\varphi_R = -30°$) presents minimum values up to 45% lower than the JWC_{51} configuration ($\delta_R = -5°$, $\varphi_R = -10°$). So it can be concluded that the induced drag coefficient decreases as the distance of the rear wing and the height of the rear wing increase.[27]

In summary, it can be stated that the configurations with the rear wing sweep angle, $\varphi_R = -30°$, are those with minimum values of drag and induced drag coefficients. On the other hand, as shown in Figure 16, the JWC_{55} configuration is the one with the best performance, as it gives the maximum aerodynamic efficiency and the maximum value of $C_L^{3/2}/C_D$, implying the minimum required power, which, as it is known, implies the best endurance and range.

Acknowledgements

The authors wish to thank the technical staff in IDR-UPM for their contribution.

Special thanks to Dr José Meseguer recently deceased, who has been a constant source of encouragement and methodological orientation. Rest in peace.

Declaration of conflicting interests

The authors declared no potential conflicts of interest with respect to the research, authorship, and/or publication of this article.

Funding

The authors received no financial support for the research, authorship, and/or publication of this article.

References

1. Chambers JR. Innovation in flight: Research of the NASA Langley Research Center on Revolutionary advanced concepts for aeronautics. NASA SP 4539, 2005.
2. Cuerno-Rejado C, Alonso-Albir L and Gehse P. Conceptual design of a medium-sized joined-wing aircraft. *Proc IMechE, Part G: J Aerospace Engineering* 2010; 224: 681–696.
3. Frediani A, Balis Crema L, Chioccia G, et al. Development of an innovative configuration for transport aircraft; a project of five Italian Universities. In: *XXVII Congresso AIDAA*, Roma, 2003.
4. Mannings R. The Future, by AIRBUS. AIRBUS Industrie, 2011.
5. Wolkovitch J. The joined wing - An overview. *J Aircraft* 1986; 23: 161–178.
6. Smith SC and Stonum RK. Experimental aerodynamic characteristics of a joined-wing research aircraft configuration. NASA TM 101083, 1989.
7. Nangia R, Palmer M and Tilmann C. Unconventional high aspect ratio joined-wing aircraft incorporating laminar flow. In: *Proceedings of the 21st AIAA applied aerodynamics conference,* Orlando, FL, USA, AIAA paper 3927-3943, 2003.
8. Rasmussen CC, Canfield RA and Blair M. Joined-wing sensor-craft configuration design. *J Aircraft* 2006; 43: 1470–1478.
9. Oligney B, Frash M and Yechout T. Aerodynamic evaluation and optimization of the Houck joined wing aircraft. In: *Proceedings of the 46th AIAA aerospace sciences meeting and exhibit*, Reno, Nevada, USA, AIAA paper 1422-1433, 2008.
10. Kroo I, Gallman J and Smith S. Aerodynamic and structural studies of joined-wing aircraft. *J Aircraft* 1991; 28: 74–81.
11. Wai JC, Herling WW and Roetman EL. Joined wing configuration aerodynamics. In: *Proceedings of the 20th AIAA/ICAS Congress*, Sorrento, Napoli, Italy, AIAA paper 2579-2589, 1996.
12. Gallman J, Smith S and Kroo I. Optimization of joined-wing aircraft. *J Aircraft* 1993; 30: 897–905.
13. Prandtl L. Induced drag of multiplanes. NACA TN 182, 1924.
14. Munk MM. General biplane theory. NACA TR 151, 1923.
15. Demasi L, Monegato G, Dispace A, et al. Minimun induced drag theorems for joined wings, closed systems, and generic biwings. In: *Proceedings of the 56th AIAA structures, structural dynamics, and materials conference,* Kissimmee, FL, USA, AIAA paper 0697-0730, 2015.
16. Wolkovitch J. Subsonic VSTOL aircraft configurations with tandem wings. *J Aircraft* 1979; 16: 605–611.
17. Kroo I. *Nonplanar wing concepts for increased aircraft efficiency*. Innovative Configurations and Advanced Concepts for Future Civil Aircraft, von Kármán Institute for Fluid Dynamics, Lecture Series, 2005.

18. Samuels MF. Structural weight comparison of a joined wing and a conventional wing. *J Aircraft* 1996; 19: 485–491.
19. Mamla P and Galinski C. Engineering notes: Basic induced drag study of the joined-wing aircraft. *J Aircraft* 2009; 46: 1438–1444.
20. Barlow J, Rae Jr WH and Pope A. *Low-speed wind tunnel testing*. New York: Wiley Interscience, 1999.
21. Stearman R, Lin H and Jhou J. Influence of joint fixity on the aeroelastic characteristics of a joined wing structure. In: *Proceedings of the 31st structures, structural dynamics and materials conference*, Long Beach, CA, USA, AIAA paper 1442-1454, 1990.
22. Cuerva A, Sanz-Andrés A, Meseguer J, et al. An engineering modification of the blade element momentum equation for vertical descent: An autorotation case study. *J Am Helicopt Soc* 2006; 51: 349–354.
23. Ministry of Defence: The Development, Concepts and Doctrine Centre. *Joint doctrine note 3/10: Unmanned aircraft systems: Terminology, definitions and classification*. 2010 (Swindon, Wiltshire, SN6 8RF, UK).
24. Bagwill TL and Selberg BP. Aerodynamic investigation of joined wing configurations for transport aircraft. In: *Proceedings of the 14th applied aerodynamics conference*, New Orleans, LA, USA, AIAA paper 30-41, 1996.
25. Letcher JS. V-Wings and diamonds ring-wings of minimum induced drag. *J Aircraft* 1972; 9: 505–607.
26. DeYoung J. Induced drag ideal efficiency factor of arbitrary lateral-vertical wing forms. NASA CR 3357, 1980.
27. Demasi L. Induced drag minimization: A variational approach using the acceleration potential. *J Aircraft* 2006; 43: 669–680.

Appendix

Notation

b	effective span
b_F	forward wingspan
b_R	rear wingspan
B	rear-forward span ratio
$\bar{c}$	effective wing mean aerodynamic chord
c_{rF}	forward wing root chord
c_{rR}	rear wing root chord
c_{tR}	rear wing tip chord
C_D	drag coefficient
$\overline{C_D}$	normalized total drag coefficient value
C_{Di}	induced drag coefficient
$\overline{C_{Di}}$	normalized induced drag coefficient value
$C_{D_{\min}}$	minimum drag coefficient
C_L	lift coefficient
$\overline{C_L}$	normalized lift coefficient value
$C_{L_{\max}}$	maximum lift coefficient
D	aerodynamic drag
e	induced drag efficiency factor
e_t	theoretical induced drag efficiency factor partial span diamond boxwing
E	aerodynamic efficiency coefficient
$E_{\max}$	maximum aerodynamic efficiency coefficient
f	frequency measuring
f_U	frequency measuring turbulence intensity
h_t	height between wings
$\overline{h_t}$	dimensionless height between wings value
$h_{t\mathrm{JWC}_{15}}$	height between wings for JWC_{15} configuration
H	dimensionless maximum height value
I_{Ux}	turbulence intensity distribution
l_t	distance between wings
$\overline{l_t}$	dimensionless distance between wings value
$l_{t\mathrm{JWC}_{15}}$	distance between wings for JWC_{15} configuration
l_F	forward wing non-projected semi-length
L	aerodynamic lift
M_y	pitching moment
q	dynamic pressure
Re	Reynolds number
S_F	forward wing area
S_R	rear wing area
T	time measuring
T_U	time measuring turbulence intensity
U	velocity measuring
U_U	velocity measuring turbulence intensity
(x, y, z)	mock-up coordinates system
(x_T, y_T, z_T)	tunnel coordinates system
α	angles of attack
δ_F	forward wing dihedral angle
δ_R	rear wing dihedral angle
λ_F	forward wing taper ratio
λ_R	rear wing taper ratio
Λ	effective aspect ratio
Λ_F	forward wing aspect ratio
Λ_R	rear wing aspect ratio
φ_F	forward wing sweep angle
φ_R	rear wing sweep angle